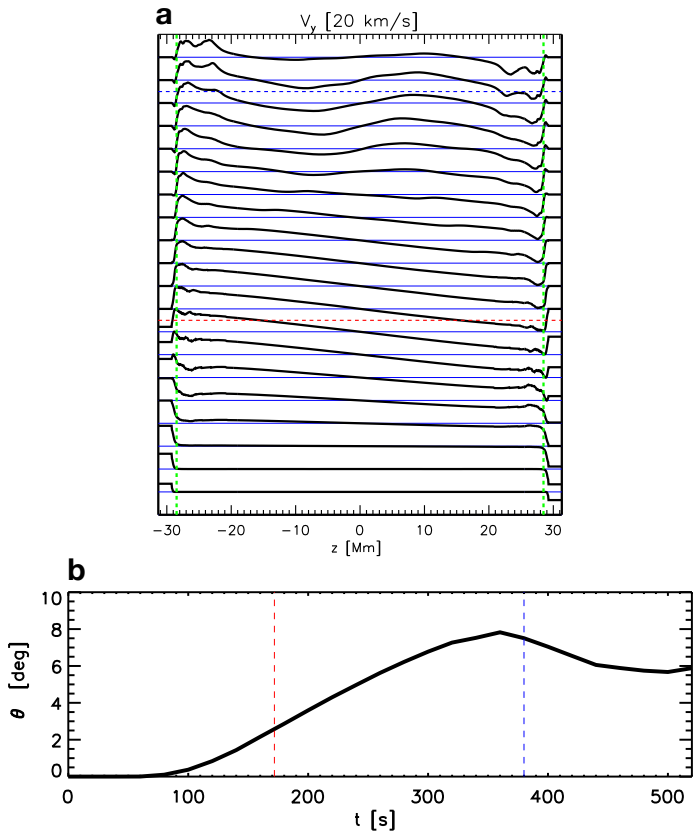

Supplementary Figure 8: **Evolution of the V_y component and tilt angle between the loops**. The top panel shows a stacked evolution every 20 s of the average V_y along the loop placed in $x < 0$ (green magnetic field lines), shown in Supplementary Fig. 19 as a B_z flux contour. The V_y range is between ± 20 km/s. The green vertical dashed lines limit the coronal part of the domain. The dashed red and blue lines in both panels represent, respectively, the time when the driver stops and the time when the reconnection occurs. Near the end of action of the driver the coronal part of the loop starts to show a V_y component that is positive over the $z > 0$ part of the loop and negative over the $z < 0$ part. This V_y component gradually increases in amplitude and also covers a larger region of the loop in the corona. The average V_y of the loop shows indications of an oscillatory behaviour. The bottom panel shows the tilt angle of the magnetic field of the loop at the apex (see text for details).

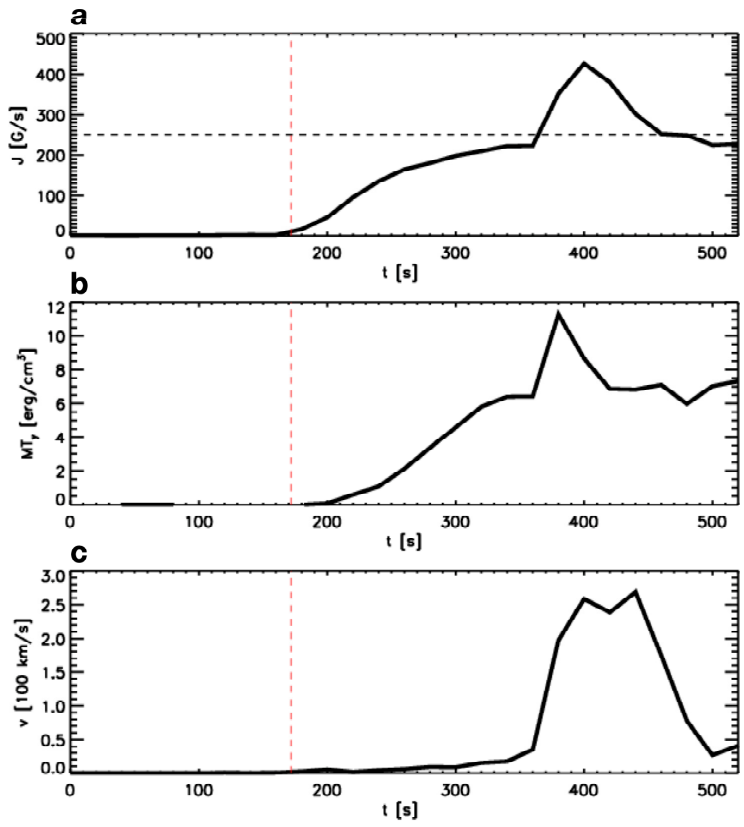

Supplementary Figure 9: **Maximum electric current (top), magnetic tension (middle) and V_y (bottom) at the jet location.** We compute these quantities along the cut $x = 0$ from $y = 0$ to the positive y-boundary. Along this cut, values of magnetic tension and V_y are positive, while we find negative but equally high values on the cut from $y = 0$ to the negative y-boundary. The horizontal black dashed line in the top panel corresponds to the current density value above which the anomalous magnetic resistivity is triggered. The vertical dashed red line marks the time when the driver stops.

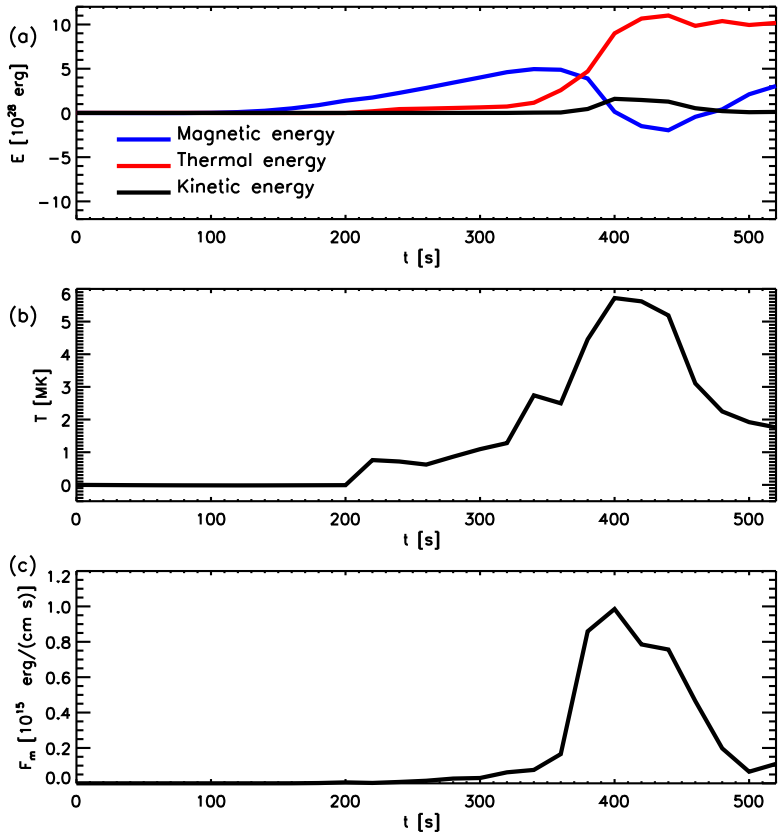

Supplementary Figure 10: **Evolution of energies and temperature in the reconnection region (relative to initial values).** The magnetic, thermal and kinetic energies (panels a) are integrated in a volume near the centre of the domain that contains the region where the jet develops. The volume extends in the $x-$direction from $x = -0.64$ Mm to $x = +0.64$ Mm, in $y-$direction from $y = -4$ Mm to $y = 0$ Mm, and in $z-$direction from $z = -2.6$ Mm to $z = +2.6$ Mm and quantities are shown with respect to their value at $t = 0$ s. The temperature (panel b) corresponds to the maximum temperature in the same volume. The electromagnetic energy inflow rate into the reconnection region (panel c) corresponds to Eq. 4.

Expansion and thinning of the loop. In Supplementary Fig. 11 we show the time-distance diagram for several transverse cuts across the loop-like structure. At time $t \approx 60$ min into the co-observation the loop started an accelerated vertical expansion. The amount of expansion is minimal close to the footpoints (cut 'H') and maximal at the apex (cut 'A'), reaching speeds of 5 km s^{-1} for the upper part of the loop. We also notice that the lower part expands faster than the upper part, reaching speeds of ≈ 15 km s^{-1}. Importantly, note that the microjets and intensity bursts happen first at the lower part of the loop and move rapidly outward with a similar rate as that observed for the motion of the lower part of the loop. This results in the thinning of the loop, observed not only in the UV passbands but also in the AIA EUV passbands. Hence, the faster accelerated expansion of the lower part may only be apparent and may actually correspond to a cancellation and/or redistribution of magnetic flux associated with the reconnection events.

EUV signatures of microjets during the expansion. In Supplementary Figs. 12 to 14 we present the UV (corresponding to the IRIS channels) and EUV signatures (corresponding to the AIA channels) of some microjets along cuts 'D' to 'I', respectively (see Supplementary Fig. 11 for a context image of the cuts). The plasmoid ejections in cuts 'D' and 'E' can be well seen across all channels, as well as several short lived (vertical or almost vertical structures in the figures) and small ($1'' - 2''$) bright features corresponding to the microjets. The plasmoid ejections along cuts 'D' and 'E' have POS velocities of $50 - 60$ km s^{-1}. Note that these ejections are strongly decelerated after traveling a distance of $d \approx 5''$. The outward transverse displacement of the entire loop is on average $8 - 15$ km s$^{-}1$, but internally, the displacement of strands can be much faster, up to 40 km s^{-1}, as seen in Supplementary Fig. 13 along cut 'F'. A common feature to all these cuts is

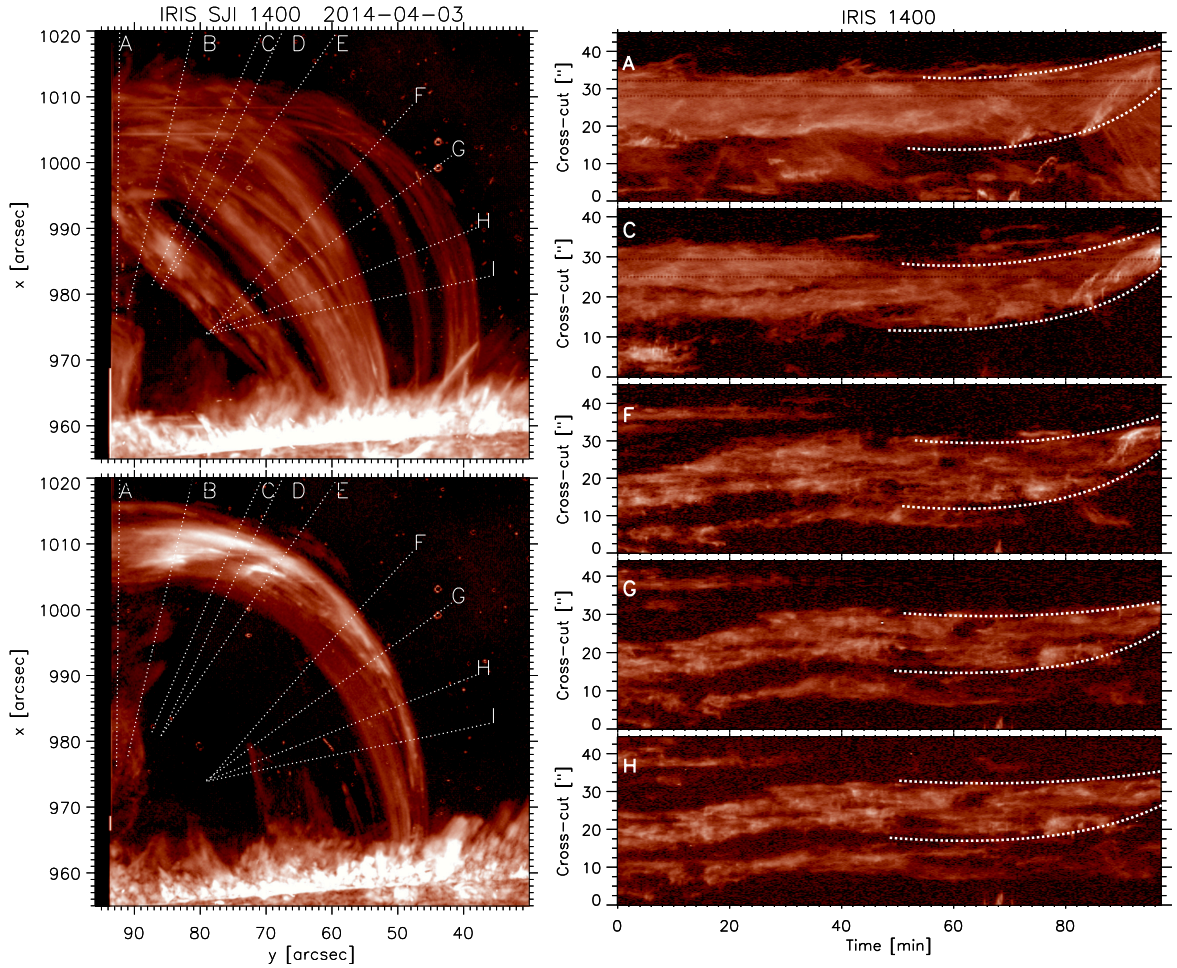

Supplementary Figure 11: **Differential expansion of the loop.** The top and bottom panels on left show, respectively a variance image over the first and last 18 min of observation. We take 8 cuts (labelled 'A' to 'I') that are roughly perpendicular to the main loop. The time-distance maps on the right show the change in time of the structure along some of these cuts. In white dotted curves we delineate the accelerated expansion of the loop. Note that this expansion is more pronounced at the apex (cut 'A') than towards the footpoints (cut 'H'). Also note that the upper part of the loop expands more slowly than the lower part.

the brightening in all intensity channels during the expansion and particularly towards the end of the observation. Note that the region across the loop that brightens is more confined in time and space for hotter channels, with the increase of intensity in the hot channels occurring slightly later in time (in a timescale of 1 min or so), suggesting progressive heating. This trend is also observed in the light curves of Supplementary Fig. 6a (see also Methods). This timelag is clearer for cuts around the middle to the footpoints of the loop, rather than at the apex, suggesting a propagation of energy from apex to footpoints. This trend can also be seen in the movie of Supplementary Fig. 1.

Further examples of the spectral signatures of microjets In Supplementary Fig. 15 we provide further examples of the spectral signatures of microjets captured by the *IRIS* spectrograph. Besides the broad, highly blueshifted component at speeds at or above 100 km s^{-1} note the presence of a redshifted component at speeds of 50 km s^{-1}. Note also that these excursions (in particular the high blueshifts) are sporadic, reminiscent of the clumpy nature of coronal rain.

Microjets prior to the expansion Much prior to the expansion of the loop, 85 min ($t \in [3, 10]$ min) and 50 min ($t \in [31, 40]$ min) before, 2 other clustered occurrences of microjets can be seen (Supplementary Fig. 16). The cluster at $t \in [31, 40]$ min occurs in the same loop and similar location as the main microjets during the expansion (close to the apex and at the bottom of the loop). For this case the trajectories in the time-distance diagram (cut 'B') are mostly slanted (with speeds of $\approx 30 - 35$ km s^{-1}) with no vertical structures, suggesting slower dynamics. At higher resolution with SOT the microjet and subsequent displacement of the strand can be traced in the POS, and result in a speed of $40 - 60$ km s^{-1} (see left panels in Supplementary Fig. 17). Note that this

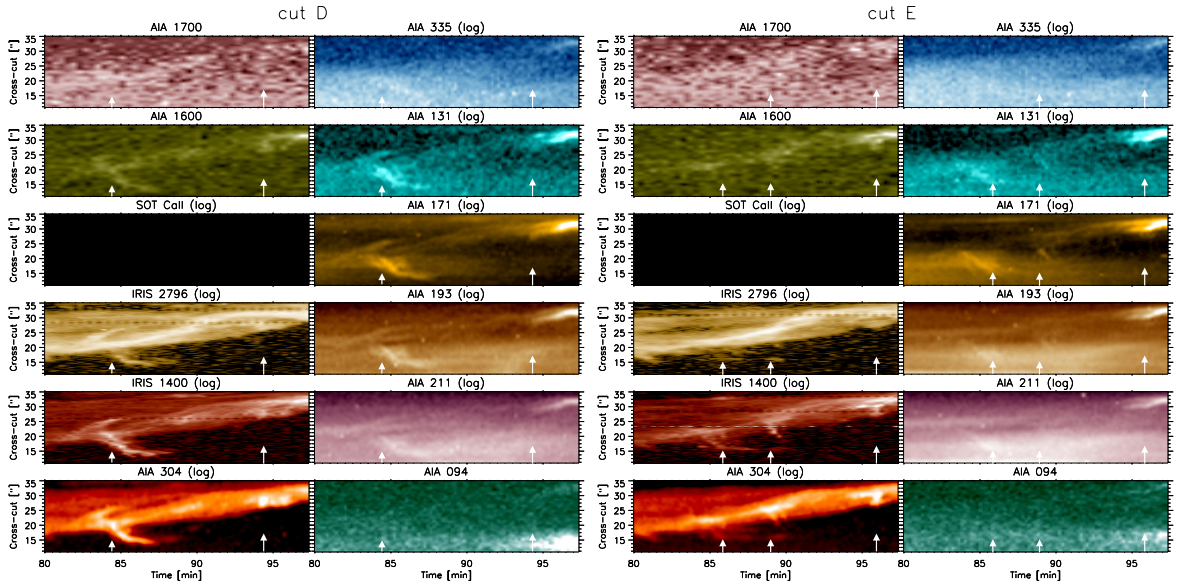

Supplementary Figure 12: **EUV signatures of microjets and plasmoids - cuts 'D' (left) and 'E' (right)**. We show time-distance maps along part of cuts 'D' and 'E' (specified in Supplementary Fig. 11) for all AIA and SJI channels during the expansion of the loop (SOT stopped observing at this time). These cuts trace part of the first clustered appearance of microjets and the ejection of plasmoids. Note that bright and small vertical features common to many channels correspond to short lived microjets (which may only live for one snapshot). Some of these features are indicated by white (or black) arrows.

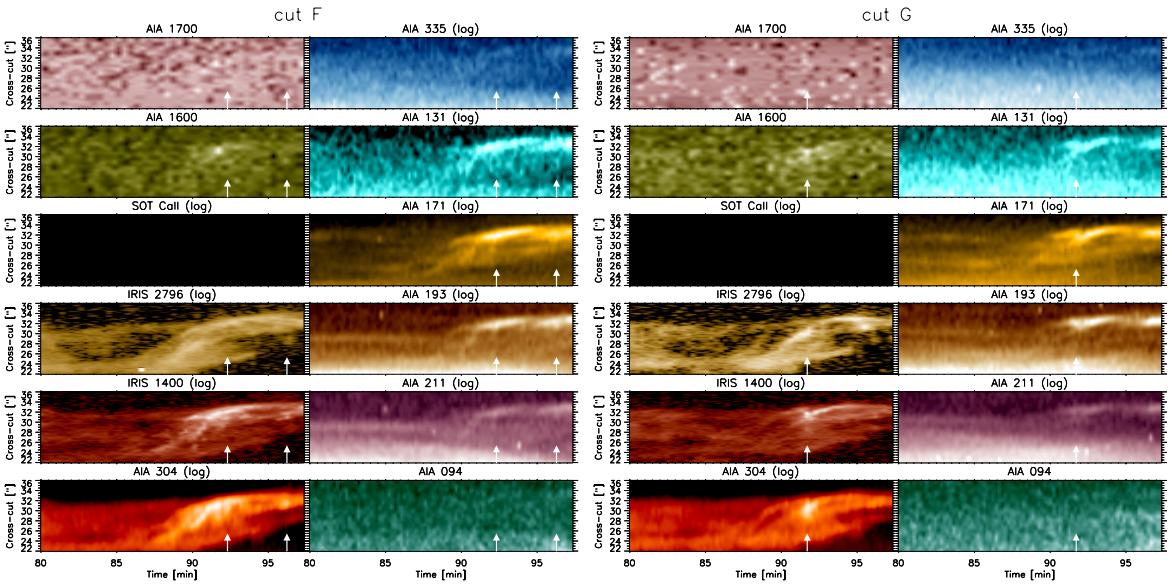

Supplementary Figure 13: **EUV signatures of microjets - cuts 'F' and 'G'.** Same as in Supplementary Fig. 12 but for cuts 'F' and 'G'. See Supplementary Fig. 11 the full view of these cuts.

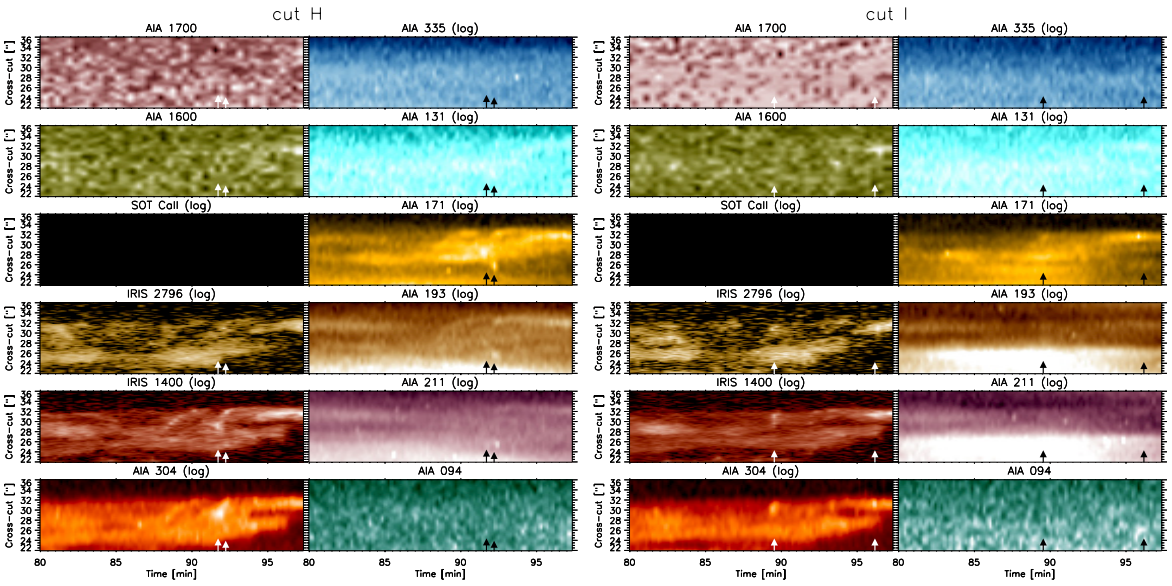

Supplementary Figure 14: **EUV signatures of microjets - cuts 'H' and 'I'.** Same as in Supplementary Fig. 12 but for cuts 'H' and 'I'. See Supplementary Fig. 11 the full view of these cuts.

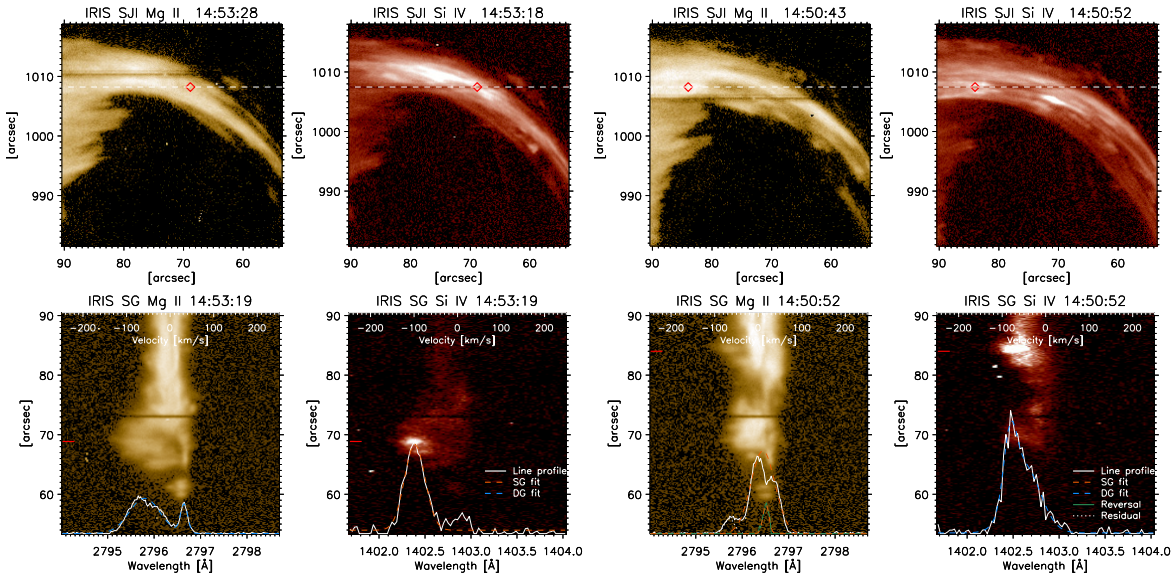

Supplementary Figure 15: **Spectral signatures of microjets - examples 2 and 3.** Similarly to Fig. 4, we show here other 2 examples of the spectral signatures of microjets. In these examples, and in particular the example on the left, in addition to the large blueshifts, redshifted components can also be seen. Note that this second redshifted component is not captured by the automatic fitting routine in the case of the Si IV line due to the low SNR. For the example on the right the fit corresponding to the red mark captures a broad optically thick main component (whose reversal is also fitted with a single Gaussian) and a small blueshifted component (residual in white dotted line). This small blueshifted component is the main component in the double Gaussian fit to the Si IV line.

displacement can also be seen in SJI 2796. Although a small EUV signature can be seen in AIA 171 (and AIA 131) after the microjets occurrence, none or almost no trace can be seen in the hotter lines. Overall, the reconnection sequence for this case is less energetic, with lower dynamics and almost no heating to coronal temperatures.

The second event at $t \in [3, 10]$ min occurs in another leg of the prominence seen in Supplementary Fig. 16 below the main loop (see also Supplementary Fig. 1 for context), only present during the first 20 min and disappearing shortly after the microjets occur. In this case the microjets show a variety of angles to the leg, from perpendicular to vertical in the POS (roughly 45° angle to the leg). Following one of these trajectories (cut 'C') we see that the microjets are roughly $2''$ in length, occur mostly only during one snapshot (producing vertical structures in the time-distance diagram) suggesting similar morphology and dynamics to the main microjets during the expansion. In Supplementary Fig. 17 the visible, UV and EUV signatures of the microjets along this cut can be seen. Note that, contrary to the previous case, this microjet cluster cannot be seen in SJI 2796 nor Ca II H, indicating temperatures out of this bandpass. The microjets are mostly vertical in the time-distance diagram in SJI 1400 and AIA 304 (indicating speeds of $140 - 180$ km s^{-1} in the POS) and the ejected plasma can be followed in the hotter EUV channels traveling at high (but lower) speeds ($70 - 100$ km s^{-1}), indicating heating of the outflow. Overall, this microjet cluster is similar in terms of dynamics and heating to the main microjets observed during the expansion, and therefore the reconnection sequence has similar energetics.

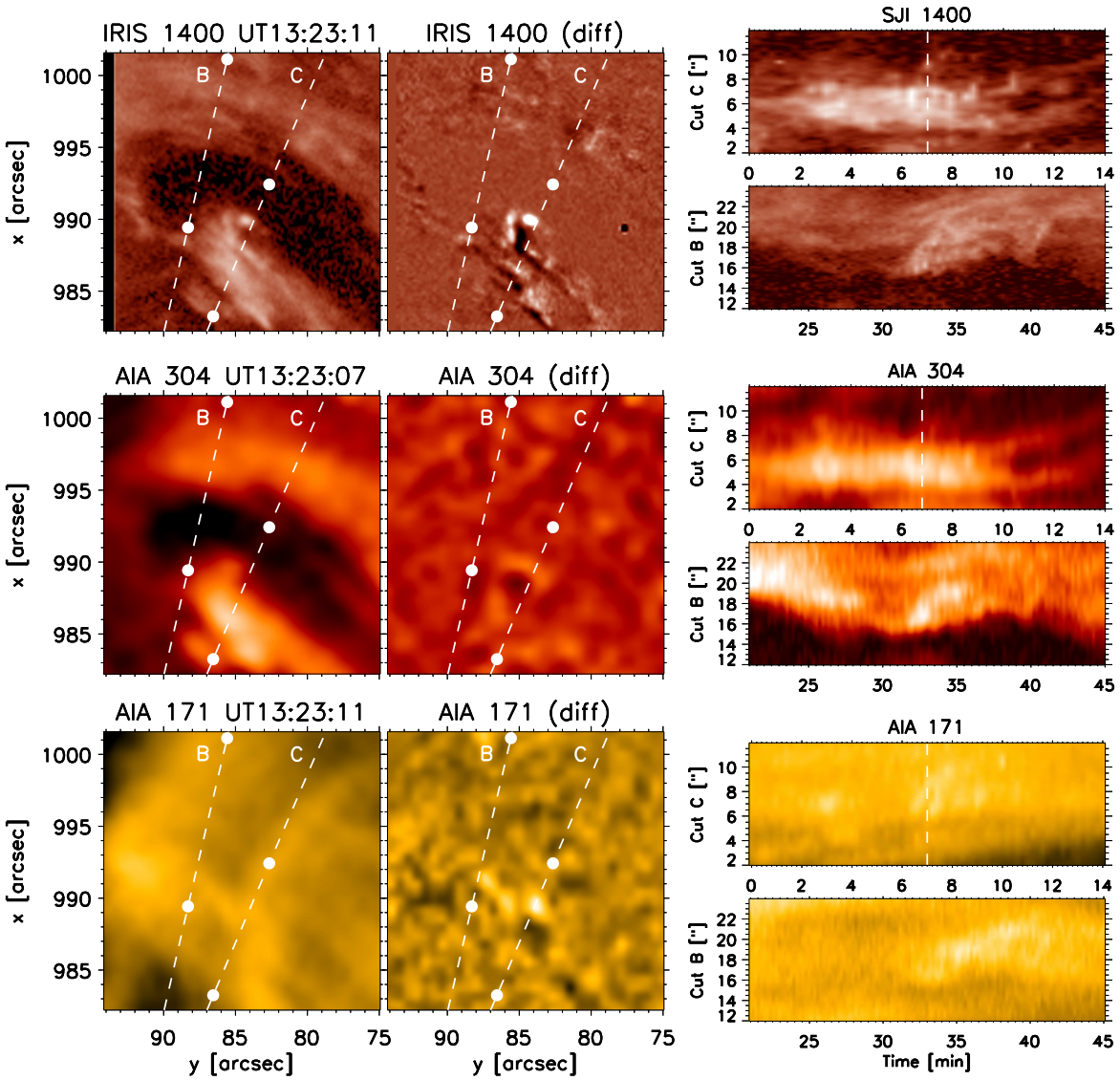

Supplementary Figure 16: **Microjets prior to loop expansion.** Same as in Fig. 2 but for 2 clusters of microjets occurring much prior to the expansion. The first cluster (cut 'C') occurs in another leg of the prominence present at the beginning of the observation. The second cluster (cut 'B') occurs in the same loop as the main studied events in this work. The microjets in the case of cut 'C' correspond to the several small vertical bright structures, living for only one snapshot. An animation of this figure is available online.

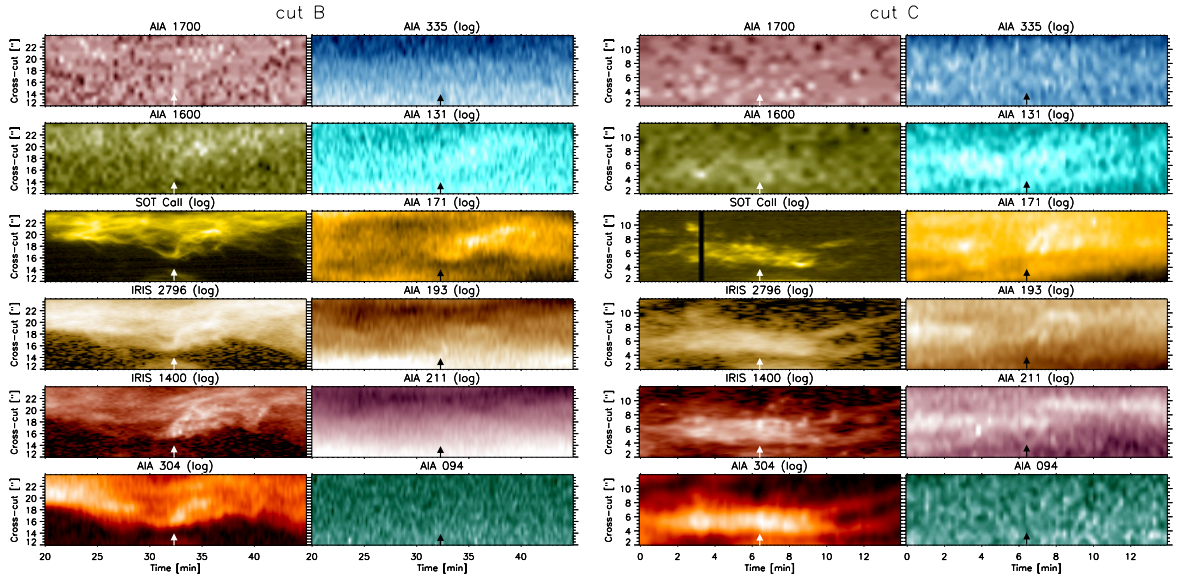

Supplementary Figure 17: **EUV signatures of microjets prior to expansion - cuts 'B' and 'C'** Same as in Supplementary Fig. 12 but for cuts 'B' and 'C'. Note the strong transverse displacement at a speed of ≈ 50 km s^{-1} associated with a microjet captured by SOT.

Numerical model As mentioned in the Methods section, the initial conditions consist of a pair of flux tubes in a gravitationally stratified atmosphere with enhanced magnetic field representative of coronal loops. The loops are allowed to relax prior to the onset of the driver. The following set of MHD equations are solved with the PLUTO code [37].

$$\frac{\partial \rho}{\partial t} + \vec{\nabla} \cdot (\rho \vec{v}) = 0, \tag{5}$$

$$\frac{\partial \rho \vec{v}}{\partial t} + \nabla \cdot \left(\rho \vec{v} \vec{v} - \vec{B}\vec{B} + p_t \mathbf{I} \right) = \rho \vec{g}, \tag{6}$$

$$\frac{\partial \vec{B}}{\partial t} \nabla \cdot \left(\vec{v}\vec{B} - \vec{B}\vec{v} \right) = -\nabla \times \left(\eta \cdot \vec{J} \right), \tag{7}$$

$$\frac{\partial E}{\partial t} + \nabla \cdot \left((E + p_t)\, \vec{v} - \vec{B} \left(\vec{v} \cdot \vec{B} \right) \right) = \rho \vec{v} \cdot \vec{g} - n_e n_H \Lambda(T) + H - \nabla \cdot \vec{F_c} - \nabla \cdot \left[\left(\eta \cdot \vec{J} \right) \times \vec{B} \right], \tag{8}$$

where t is time, $\vec{v}$ the velocity, p_t the total pressure, i.e. the sum of gas pressure p and magnetic pressure p_m, $\vec{B}$ the magnetic field, $J = \frac{c}{4\pi} \nabla \times \vec{B}$ the current density, c the speed of light, and $\mathbf{I}$ the identity tensor. The total energy density E is given by

$$E = \frac{p}{\rho(\gamma - 1)} + \frac{1}{2}\vec{v}^2 + \frac{\vec{B}^2}{8\pi\rho}, \tag{9}$$

where $\gamma = 5/3$ denotes the ratio of specific heats. We also have the mass density ρ, and $\mu = 1.26$ the mean atomic mass that together with the mass of the proton m_H is used to derive the

electron density n_e and the number density n_H. We assuming solar metal abundances [38]. The gravity acceleration vector is the projection of the vertical solar gravity vector $g_\odot$ onto the assumed direction of the loop axis.

In the energy equation T is the temperature and $\vec{F}_c$ is the anisotropic energy flux due to thermal conduction [39], where we also consider a saturation effect. This thermal conduction term is solved separately from the advection terms using the super-time-stepping technique [40]. The optically thin radiative loss function $\Lambda(T)$ is computed with the aid of the CHIANTI code [Version 7, 41], where we assume a density of 10^9 cm^{-3} and a ionisation equilibrium according to [42].

An artificial broadening of the temperature gradient in the transition region is obtained to describe properly the energy exchange between chromosphere and corona without the need of increasing spatial resolution. The broadening has been achieved by imposing the thermal conductivity $k(T)$, parallel to the field lines, to be constant below a critical temperature T_c (here fixed at 0.25MK), and by modifying the radiative losses function $\Lambda(T)$ so that the product $k(T)\Lambda(T)$ is a constant [43, 44, 45, 46].

The heating term H is maintained constant and equal to the plasma radiative losses at $t = 0$. We do not impose a magnetic field divergence cleaning, since the magnetic field evolution is computed using the constrained transport approach [47]. Finally, we consider an anomalous magnetic resistivity η, given by $\eta = \eta_0$ where $|\vec{J}| > J_0$ and $\eta = 0$ elsewhere. In our simulation we use an electric current threshold of $J_0 = 250$ G s^{-1} and a magnetic resistivity value of $\eta_0 = 10^{14}$ cm^{-2} s^{-1}. This current threshold is between 2 and 3 orders of magnitude larger than the value

of the electric current at $t = 0$ s.

Initial conditions of the numerical simulation The initial magnetic field connects two chromospheric regions at opposite z-extrema of our domain, with a corona in between and two steep transition regions connecting the chromospheres to the corona. The magnetic field is only along the z-direction and is described by the following lorentz profile:

$$B_z(x, y, z) = B_0 + \sum_{i=1}^{2} B_{z0} \frac{1}{r_i^2(x, y)/\sigma^2 + 1} \tag{10}$$

where B_0 is the ambient magnetic field (15 G), B_{z0} is the amplitude (300 G), σ is the width (250 km), and r_i is a distance ($\sqrt{(x - x_i)^2 + (y - y_i)^2}$). This configuration is out of equilibrium and there are two regions with excess magnetic pressure around the two flux tube axes centred at $(x_i, y_i) = (-2, 0)$ Mm and $(2, 0)$ Mm. This excess leads to an initial expansion of the magnetic field around these axes and a consequent rarefaction of the plasma inside the expanding flux tubes. To avoid such rarefaction, an excess of density and pressure has been imposed in the corona, with the same profile as for the magnetic field:

$$\rho(x, y, z) = (\sum_{i=1}^{2} \frac{9}{r_i^2(x, y)/\sigma^2 + 1} + 1)\rho_{loop}(z) \tag{11}$$

$$p(x, y, z) = (\sum_{i=1}^{2} \frac{9}{r_i^2(x, y)/\sigma^2 + 1} + 1)p_{loop}(z) \tag{12}$$

where $\rho_{loop}(z)$ and $p_{loop}(z)$ are the density and pressure of a hydrostatic loop by [48, see also

[49]].

Because of the different β regimes of the corona and the chromospheric regions, the final configuration shows a largely expanded, vertical magnetic field in the corona while it remains rather unchanged in the chromospheric regions and a strong expansion across the transition regions.

The magnetic field expansion is symmetric around $x = 0$ where the two flux systems (i.e. loops) co-exist. We take as $t = 0$ the time after relaxation, when the two loops are in pressure balance and have stopped evolving. At this time the magnetic field in the corona settles to a value of approximately 15 G. Supplementary Fig. 18a illustrates the configuration of the two loops at the end of the relaxation with iso-contours of B_z flux and some representative magnetic field lines. Supplementary Fig. 18b and 18c show the distribution of density ρ and temperature T after relaxation on the $x - z$ plane at $y = 0$, i.e. across the centre of the loops. Both ρ and T mostly show variations along the $z-$direction and only minor variations along x. The distributions show structures revealing the footpoints of the loops.

Driver phase in the numerical simulation. In the next step of the simulation, a footpoint driver is applied from $t = 0$ so that the magnetic field evolves into a configuration that is likely to lead to the magnetic reconnection between the loops. The driver is given by:

$$V_y = V_{max} \sin \frac{t}{\tau} 2\pi \tag{13}$$

and acts only for $t < \tau/2$. In our simulation $V_{\max} = 20$ km s^{-1}, and $\tau = \Delta y / V_{\max} \pi$ where we fix $\Delta y = 2.2$ Mm, corresponding to the maximum separation of the footpoints. The driver is applied

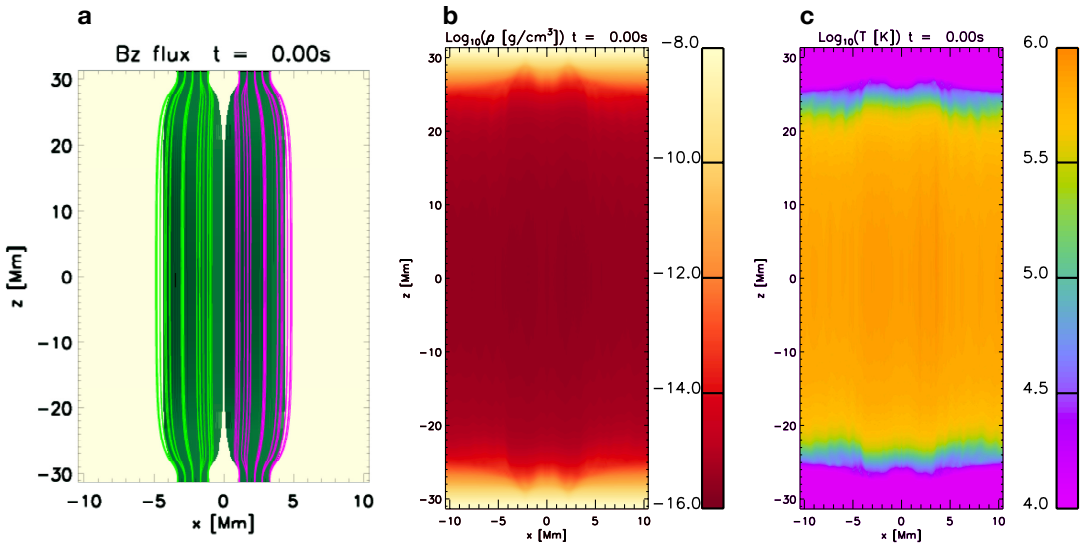

Supplementary Figure 18: **Initial conditions of the numerical model.** We show the configuration at $t = 0$ of the 2 loops configuration with the iso-surface of B_z flux and overplotted magnetic field lines (panel **a**), the map of $Log_{10}(\rho)$ (panel **b**) and $Log_{10}(T)$ (panel **c**) in the plane $y = 0$.

to both entire chromospheric regions and in opposite directions for the two loops. That is, for one loop the footpoints at the lower and upper z-boundaries of the simulation are displaced with a positive and negative velocities, respectively. We invert the velocities for the other loop. It is meant to translate the loops footpoints so as to tilt them with respect to one another by about 4°.

This dynamic leads to an x-shaped configuration of the two loops when seen on the $y - z$ plane. Following the motion of the footpoints, the magnetic field in the corona responds by developing a y-component.

Supplementary Fig. 19 shows this evolution, where the loops are illustrated on the $y - z$ plane and thus are along the same line-of-sight at $t = 0$ (panel **a**). As the footpoints move, the tilt between the two loops becomes larger. At $t = 180$ s the driver stops and the footpoints are maximally displaced (panel **b**). However, the coronal magnetic field does not immediately adjust to the new boundary conditions and it continues evolving towards a new equilibrium. At $t = 380$ s, the magnetic field in the corona has changed with respect to $t = 180$ s and shows a greater tilt between the two loops (panel **c**).

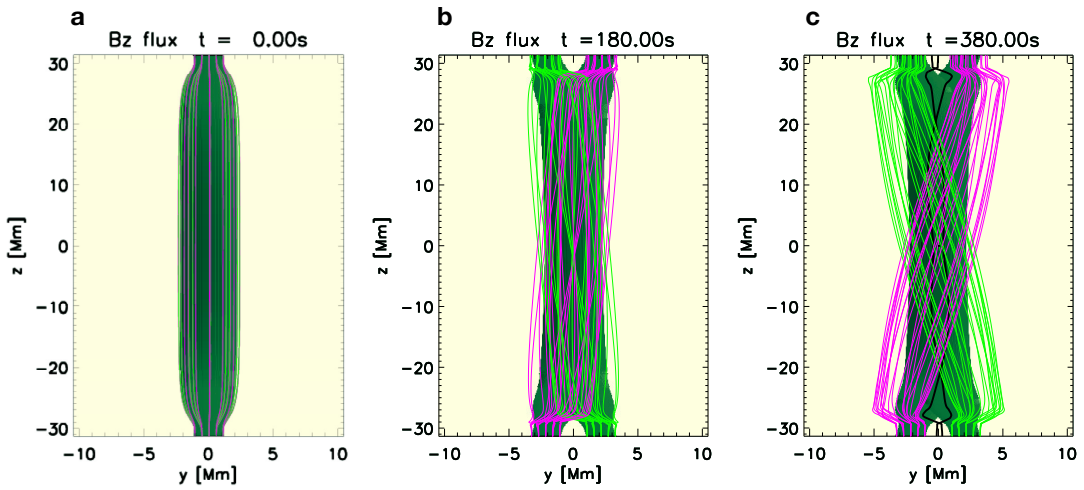

Supplementary Figure 19: **Configuration of the system prior to reconnection.** We show the configuration of the system at $t = 0$ (panel **a**), $t = 180$ s (panel **b**) and $t = 380$ s (panel **c**), just prior to the time when the reconnection starts and the jet is triggered. In all panels we display magnetic field lines representative of the 2 loops (magenta and green) and an iso-contour of B_z flux that highlights how the loop structures expand in the corona.